LA-UR-17-31015
Approved for public release; distribution is unlimited.

Title: SURFplus Model Calibration for PBX 9502

Author(s): Menikoff, Ralph

Intended for: Report

Issued: 2017-12-06

SURFplus model calibration for PBX 9502

Ralph Menikoff

December 4, 2017

Abstract

The SURFplus reactive burn model is calibrated for the TATB based explosive PBX 9502 at three initial temperatures; hot (75 C), ambient (23 C) and cold (-55 C). The CJ state depends on the initial temperature due to the variation in the initial density and initial specific energy of the PBX reactants. For the reactants, a porosity model for full density TATB is used. This allows the initial PBX density to be set to its measured value even though the coefficient of thermal expansion for the TATB and the PBX differ. The PBX products EOS is taken as independent of the initial PBX state. The initial temperature also affects the sensitivity to shock initiation. The model rate parameters are calibrated to Pop plot data, the failure diameter, the limiting detonation speed just above the failure diameters, and curvature effect data for small curvature.

1 Introduction

The SURFplus reactive burn model [Menikoff and Shaw, 2012] utilizes a fast rate for hot-spot burning and a slow rate for the energy release as carbon clusters are formed. Previously, the burn model was calibrated for the TATB based explosive PBX 9502 at ambient initial temperature (25 C) [Menikoff and Shaw, 2012]. The calibration was based on fitting Pop plot data, the failure diameter and the limiting detonation speed just above the failure diameter [Menikoff, 2017c]. Here we refine the calibration of ambient PBX 9502 using the experimental Pop plot fit from [Gustavsen et al., 2006], which differs slightly from the older values listed in [Gibbs and Popolato, 1980, p. 126], and also fit to curvature effect data, detonation speed of a curved detonation wave [Hill and Aslam, 2010], for small curvature; *i.e.*, $D_n(\kappa)$ for $\kappa \lesssim 0.25\,\mathrm{mm}^{-1}$. As discussed later the curvature effect largely determines the parameters of the slow rate.

In addition, SURFplus parameters are calibrated for hot (75 C) and cold (-55C) PBX 9502 to the same type of data as used for ambient PBX 9502. Both the CJ state and sensitivity to shock initiation depend on the initial PBX temperature. The change in the CJ state is mostly due to thermal expansion which affects the chemical energy release per unit volume. Thus the CJ detonation speed and CJ pressure decrease as the initial temperature is increased. Pop plot data indicates that the shock sensitivity increases (shorter distance-of-run to detonation for a given initial shock strength) as the initial temperature is increased. Hence, the burn rate increases with temperature. As a consequence, the failure diameter decreases with increasing temperature.

We use the same products equation of state (EOS) for hot, ambient and cold PBX 9502. There is data on the thermal expansion of the reactants; see [Skidmore et al., 2003] and references therein. To account for the thermal expansion of the PBX 9502 reactants we use a porosity model for full density TATB [Menikoff, 2009]. Given the initial reactant state (density and specific internal energy) the CJ state is determined by the Hugoniot equation and the EOS of the products. The model EOS is described and the CJ states for hot, ambient and cold PBX 9502 are given in section 2.

The SURFplus model burn parameters are fit by matching simulated results with the `xRage` code to experimental data. The data and simulated results are discussed in section 3 along with a table for the calibrated burn parameters.

We conclude with a brief summary in section 4. For completeness, the fitting form for the SURF rate [Menikoff, 2017c] is specified in the appendix A and for the SURFplus extension in appendix B.

2 Model EOS

We use the EOS models for the reactants and products described in [Menikoff, 2009]. The reactants utilize a porosity model based on an EOS for full density TATB. The TATB EOS is of the Mie-Grüneisen form with the cold curve as the reference. A Keane fitting form calibrated in part to diamond anvil cell isothermal compression data is used for the cold curve. The porosity is given by $1 - \rho_{0,PBX}/\rho_{0,TATB}$, where $\rho_{0,PBX}$ and $\rho_{0,TATB}$ are the densities at the initial state (P_0 and T_0) of PBX 9502 and TATB, respectively.

As discussed in [Menikoff, 2017b], the SESAME products EOS is scaled to better agree with the CJ detonation speed from extrapolating diameter effect data of Campbell [1984] to infinite diameter (*i.e.*, planar detonation wave). The scaled products EOS also fits cylinder test data for the release isentrope; see [Menikoff, 2017b, fig. 1]. This is the same EOS model as used in the previous calibration of ambient PBX 9502 [Menikoff, 2017c].

The reactant shock Hugoniot and products detonation loci along with data for ambient PBX 9502 are shown in fig. 1. For hot and cold PBX 9502, the same TATB EOS and products EOS are used but with the porosity adjusted to account for thermal expansion based on the work of [Skidmore et al., 2003].

For the `xRage` code, a simple ramp model with a low crush-up pressure (0.2 GPa) is used. The high pressures of interest are much greater than the yield strength of TATB. Consequently, pores

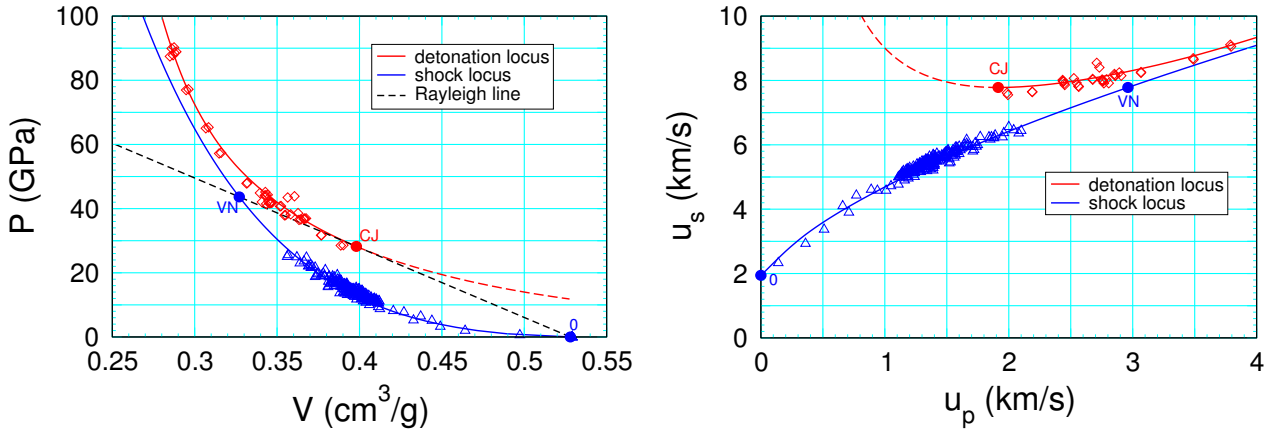

Figure 1: Reactant shock locus and products detonation locus for ambient PBX 9502 from the reactant and products EOS models. Solid and dashed red curves are for strong and weak detonations, respectively. The CJ state and the von Neumann spike state are denoted by red and blue solid circles, respectively. Blue triangles are Hugoniot data from [Dick et al., 1988] and [Gustavsen et al., 2006]. Red diamonds are overdriven detonation data from [Tang et al., 1998] and [Green et al., 1985].

are compressed out by the lead shock and the details of the porosity model are not important. The purpose of the porosity is to set the initial PBX density. This is important as the initial density affects the Hugoniot locus and the CJ state.

2.1 PBX 9502 thermal expansion

The thermal expansion of a TATB crystal is very anisotropic due to its graphite like structure with strongly bonded molecules within planes that are weakly bonded [Kolb and Rizzo, 1979]. Moreover, for polycrystal TATB compactions with a few per cent porosity, the coefficient of thermal expansion varies widely with TATB type (dry- or wet-animated crystals), compaction method (uniaxial or isostatic) and crystal size (10 to 50 microns); see [Rizzo et al., 1981, table 10] or [Skidmore et al., 2003, table 2]. In fact, the volumetric thermal expansion of a compaction can be either less than or greater than that of the single crystal.

PBX 9502 is composed of TATB grains with a Kel-F binder and a couple per cent porosity. One might expect the PBX to have a random crystal orientation of TATB grains and thus have an isotropic thermal expansion. However, when grains and binder are pressed to form the PBX, the TATB crystals partially align with the pressure gradient normal to the tightly bonded planes leading to a significant anisotropy; see [Skidmore et al., 2003], [Souers et al., 2011] and references therein. Moreover, the PBX 9502 volumetric coefficient of thermal expansion increases significantly with temperature; linear (1/3 volumetric) coefficient varies from 45e-6/K at -55 C to 130e-6/K at 75C [Skidmore et al., 2003, fig. 8].

For a fluid EOS, the volumetric coefficient of thermal expansion is given by the thermodynamic relations

$$\beta = \frac{\Gamma\, C_p}{V\, K_s} = \frac{\Gamma\, C_v}{V\, K_T} = \frac{\Gamma C_v}{V\, K_s - \Gamma^2 C_v\, T}\ , \tag{1}$$

where Γ is the Grüneisen coefficient, C_p and C_v are the specific heat at constant pressure and constant volume, respectively, and K_s and K_T are the isentropic and isothermal bulk modulus, respectively. For the TATB EOS, at the ambient state $V = 0.5149\,\mathrm{cm}^3/\mathrm{g}$, $T = 297\,\mathrm{K}$, $\Gamma = 0.5$, $K_s = 13.6\,\mathrm{GPa}$ and $C_v = 1.2\text{e-}3\,(\mathrm{MJ/kg})/\mathrm{K}$. This gives $\beta = 8.75\text{e-}5\,\mathrm{K}^{-1}$, which is low compared to the values for either crystal TATB of about $36\text{e-}5\,\mathrm{K}^{-1}$ or PBX 9502 of about $17\text{e-}5\,\mathrm{K}^{-1}$.

One could match the coefficient of thermal expansion of the TATB EOS to the measured value of PBX 9502 by lowering the ambient bulk modulus to 7 GPa. The value of the ambient bulk modulus for the EOS model is based on a fit to diamond anvil cell data; see [Menikoff, 2009]. The fitting form for the Mie-Grüneisen cold curve has sufficient degrees of freedom to lower the ambient bulk modulus and still fit the higher pressure data reasonably well. We have chosen not to do this due to uncertainties from the anisotropy and the temperature dependence

of the thermal expansion. The porosity model for the PBX allows more flexible in setting the initial density.

For a given initial pressure and temperature (P_0, T_0), the PBX parameters (initial state and porosity) are set as follows. First, one determines the TATB density and specific energy $\big(\rho_{TATB}(P_0,T_0),\, e_{TATB}(P_0,T_0)\big)$. Second one determines the PBX 9502 initial density $\rho_{PBX}(P_0,T_0)$ using a fit for the measured PBX thermal expansion as described below. The porosity is then given by

$$\text{porosity} = 1 - \rho_{PBX}(P_0,T_0)/\rho_{TATB}(P_0,T_0)\ . \tag{2}$$

For the simple ramp model used by the `xRage` code, we note that the initial specific energy of the PBX is the same as the initial specific energy for the TATB; *i.e.*, $e_{PBX}(P_0,T_0) = e_{TATB}(P_0,T_0)$.

Typically, the density of a PBX sample is measured only at ambient conditions using a water immersion technique to measure the volume. At a specified temperature, the density needs to be determined utilizing a previously measured coefficient of thermal expansion. The linear coefficient of thermal expansion (CTE), which corresponds to $\beta/3$, is defined as

$$CTE(T,P) = -\frac{1}{3\,V}\Big(\frac{\partial V(T,P)}{\partial T}\Big)_P\ . \tag{3}$$

More convenient is the average or secant based linear CTE

$$CTE_{secant}(T,P) = \frac{1}{3\,V(T_{ref},P)}\cdot\frac{V(T,P)-V(T_{ref},P)}{T-T_{ref}} \tag{4}$$

For PBX 9502, Skidmore et al. [2003, Eq. (7)] provides the following fit at $P_0 = 1\,\text{bar}$ and with $T_{ref} = 21\,\text{C}$:

$$CTE_{secant}(T,P_0) = 5.31\times10^{-5} + 1.94\times10^{-7}\,T + 2.64\times10^{-9}\,T^2 + 1.83\times10^{-11}\,T^3\ , \tag{5}$$

where T is in degrees centigrade.

The difference between the coefficients of thermal expansion for TATB and PBX 9502 causes the model porosity to change. Linearizing Eq. (2), the change in porosity is given by

$$\text{porosity}(T) = \text{porosity}(T_{ref}) - \frac{V_{TATB}(T_{ref})}{V_{PBX}(T_{ref})}\cdot\big[\bar\beta_{TATB}(T) - \bar\beta_{PBX}(T)\big]\cdot\big(T-T_{ref}\big)\ , \tag{6}$$

where $\bar\beta$ denotes the average or secant volumetric coefficient of thermal expansion. Hence the model porosity would increase with temperature if $\bar\beta_{PBX}(T) > \bar\beta_{TATB}(T)$. As discussed earlier in this subsection, the model porosity does not necessarily correspond to the physical porosity. However, except for setting the initial PBX density, at the high pressures of interest, the PBX EOS is insensitive to the porosity.

2.2 CJ Detonation

An underdriven detonation wave is determined by the initial reactant state, the products EOS, the Hugoniot equation and the sonic condition. The initial reactants state, von Neumann (VN) spike state and Chapman-Jouguet (CJ) state are listed in table 1 for hot, ambient and cold PBX 9502. The table shows the expected behavior that the detonation speed and the CJ pressure both decrease with increasing temperature.

Most of the change is due to the specific volume increasing with temperature. However, the reactants specific energy also increases with temperature and affects the CJ state. We note that the energy origin of the reactants is chosen such that the initial energy is 0 at the ambient temperature, and consequently is non-zero at higher and lower temperatures.

Table 1: CJ detonation states for hot, ambient and cold PBX 9502.

	V cm^3/g	e MJ/kg	P GPa	T K	u_p km/s	c km/s	porosity per cent
Hot (75 C)							
Init state	0.53515	0.0618	0.0001	348	0.0	1.439	3.3*
detonation speed 7.706 km/s							
VN spike	0.32871	4.4797	42.80	1666	2.973	8.094	
CJ state	0.40317	1.8674	27.36	3020	1.900	5.805	
Ambient (26 C)							
Init state	0.52798	0.0	0.0001	300	0.0	1.944	2.5
detonation speed 7.782 km/s							
VN spike	0.32706	4.3850	43.65	1586	2.961	8.131	
CJ state	0.39808	1.8331	28.22	2955	1.915	5.867	
Cold (-55 C)							
Init state	0.52214	-0.0928	0.0001	218	0.0	1.735	2.0*
detonation speed 7.838 km/s							
VN spike	0.32582	4.2498	44.24	1494	2.947	8.159	
CJ state	0.39391	1.7599	28.90	2879	1.925	5.913	

* model dependent value

Hot and cold detonation speeds are consistent with the expression for the leading order change with variations in the initial state [Fickett and Davis, 1979, §3.11];

$$\frac{\Delta D_{cj}}{D_{cj}} = -A\,\frac{\Delta V_0}{V_0} + B\,\frac{\Delta e_0}{D_{cj}^2}\ , \tag{7}$$

where

$$A = \frac{\gamma(\gamma - \Gamma - 1)}{2\gamma - \Gamma}\ , \tag{8a}$$

$$B = \frac{\Gamma}{2\gamma - \Gamma}\,(\gamma + 1)^2\ , \tag{8b}$$

and at the CJ state for the ambient initial temperature, for the 9502 products EOS model, the adiabatic index is $\gamma = 3.064$ and the Grüneisen coefficient is $\Gamma = 0.5$. This gives $A = 0.851$ and $B = 1.47$. Then the variation with density is $\Delta D_{cj} = 3.50\,(\mathrm{m/s})\,\Delta\rho_0/(\mathrm{mg/cm^3})$, and the variation with energy is $\Delta D_{cj} = 0.189\,(\mathrm{m/s})\,\Delta e_0/(\mathrm{J/g})$. For the hot temperature this gives the contribution to ΔD_{cj} from the density and energy to be -88.7 and +11.6 m/s, respectively. The total linearized change is -77.1 m/s compared to -76 m/s from table 1.

The EOS of the products was calibrated such that the ambient CJ detonation speed matches the value obtained by extrapolating diameter effect data of Campbell [1984]. Hot and cold diameter effect data only extend up to a 1 inch diameter rate stick, compared to ambient data which extend up to a 4 inch diameter. Consequently, extrapolating the detonation speed for hot and cold PBX 9502 is not as accurate. The detonation speed from the EOS is within the estimated uncertainty of the extrapolation.

3 Model rate

The burn rate is calibrated to Pop plot data, the failure diameter and limiting detonation speed, and curvature effect data. The functional form and parameters for the SURF burn rate are given in Appendix A, and the SURFplus parameters in Appendix B. First, we describe parameters that dominate the fit to particular data. The parameter are not completely independent and an iteration and trade-offs are needed for a best fit to the detonation phenomena of interest. Second, we describe the results of the calibration and comment on the issue of resolution that is used for the simulations. In the next subsection the data and the fit to the data are described.

Shock initiation is characterized by the Pop plot; distance-of-run to detonation as a function of initial shock pressure. The Pop plot data is in the pressure interval $8 \lesssim P_s \lesssim 18$ GPa. It is

Table 2: SURFplus parameters for PBX 9502; see Eq. (A.1b) and Eq. (A.3) for SURF rate parameters and Eq. (B.1) and Eq. (B.4) for carbon clustering (SURFplus) parameters.

SURF parameters

p_{scale}	1 GPa		
t_{scale}	1 μs		
parameter	hot	ambient	cold
P_0	5.0	6.0	7.0
P_{low}	7.0	8.0	8.0
P_1	30.	28.	30.
P_{hi}	55.	60.	60.
C	4.25e-4	4.6e-5	1.74e-5
f_n	3.4	4.05	4.25
n	2.4	3.2	2.8
n_{hi}	0.0	0.0	0.0
s_1	2.0	2.0	2.0
P_{burn}	15.	15.	15.

Carbon clustering parameters

parameter	hot	ambient	cold
Q		3.	
$Nratio$		50.	
t_1		0.005	
t_2	0.10	0.4	0.8
h_1		0.001	
h_2		0.95	

dominated by two parameters; c and fn in Eq. (A.3); see [Menikoff, 2017a]. Crude estimates are used for the low pressure transition parameters, p_0 and p_{low}, since there is no data below 8 GPa.

The failure diameter is dominated by the parameter n in Eq. (A.1b). The limiting detonation speed is then determined by the curvature effect; detonation speed as function of the local front curvature, $D_n(\kappa)$. For small curvature, $\kappa \lesssim 0.25\,\text{mm}^{-1}$, the detonation speed is dominated by the slow rate, hence the carbon clustering parameters. For larger curvatures, the sonic point is near the end of the fast reaction, and the detonation speed is dominated by the carbon clustering energy subtracted from the equilibrium products EOS, SURFplus parameters Q in Eq. (B.1), and the reaction width of the fast reaction which is determined by the SURF rate at high pressure, transition pressure parameters p_1 and p_{hi} in Eq. (A.3). The limiting detonation speed falls within the larger curvature regime and is not affected by the details of the carbon clustering reaction.

The parameters that best fit the data for hot, ambient and cold PBX 9502 are list in table 2. A plot of the SURF rate $f(P_s)$ for the 3 initial temperatures is shown in fig. 2. As expected, the rate increases with the initial temperature, since the lower initial density at higher temperature gives rise to a greater particle velocity for a given shock pressure and hence a higher hot-spot temperature from pore collapse. We also note that the asymptotic rate, when the number of

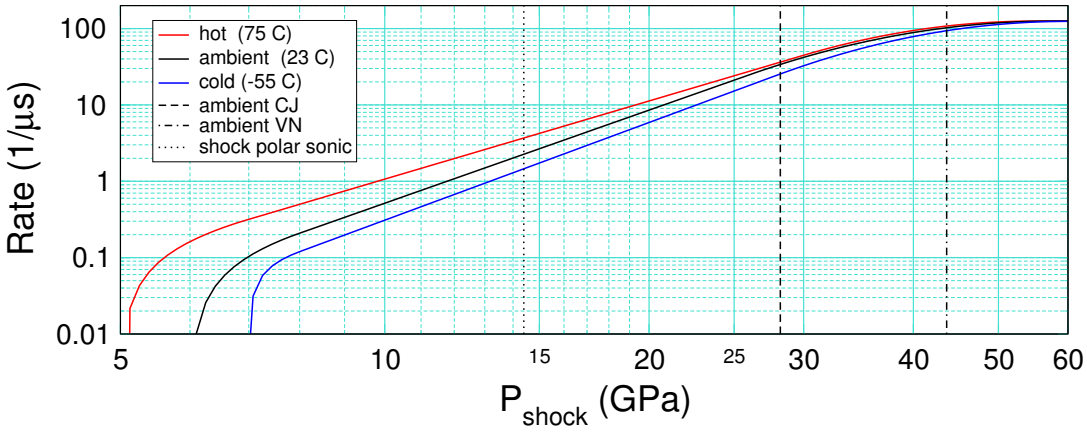

Figure 2: SURF rate $f(P_s)$ for hot, ambient and cold PBX 9502. The CJ, VN spike and shock polar sonic pressures for the ambient temperature are indicated with vertical lines.

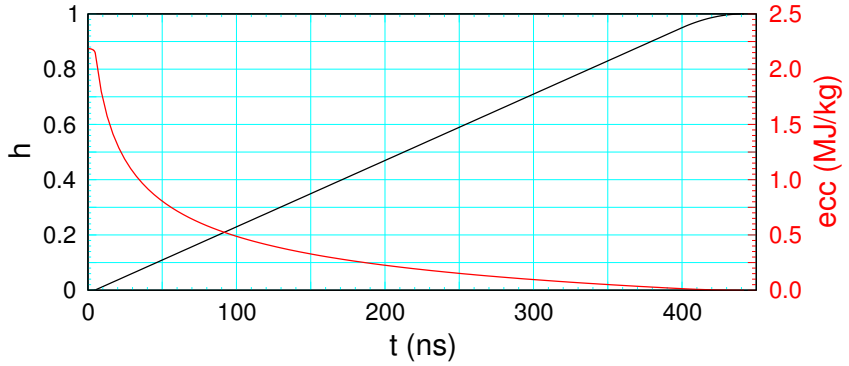

Figure 3: The limiting time dependence of the carbon clustering reaction and the carbon clustering energy for ambient PBX 9502.

hot spots saturates, is about the same. Significant pressures for a detonation wave at ambient temperature (CJ state and VN spike from table 1) are displayed as vertical lines. Also displayed is the sonic pressure on the ambient shock polar (based on the reactants EOS and the limiting detonation speed), which is the boundary pressure for unconfined rate sticks used to measure the failure diameter.

The limiting time dependence of the carbon clustering reaction for the ambient CJ detonation, $\lambda_2 = h(t)$ with Eq. (B.4) for h, and the corresponding carbon clustering energy Eq. (B.1) subtracted from the equilibrium products EOS, Eq. (B.3), are shown in fig. 3. For the carbon clustering model of Shaw and Johnson [1987], the volume of the carbon clusters grows linearly

in time and the carbon cluster energy is proportional to the inverse of the cluster radius. For the SURFplus model, the second reaction progress variable λ_2 is proportional to the cluster volume, and the cluster radius is proportional to $[N_{ratio}\,\lambda_2 + (1-\lambda_2)]^{1/3}$. We note that 40 % of the carbon cluster energy is released shortly after the end of the fast reaction, about 20 ns which corresponds to $\lambda_2 \approx 0.04$, and 80 % after about 100 ns, which corresponding to $\lambda_2 \approx 0.25$. To fit the curvature effect for hot and cold temperatures the cluster parameter t_2 is varied; see table 2.

The simulations for calibrating the model parameters used the adaptive mesh refinement code `xRage`. The setup is described in [Menikoff, 2017c]. For the fast rate, the reaction zone is refined to a cell size of 0.015 mm (1/64 mm). To illustrate the resolution, fig. 4 shows the profiles of the pressure and reaction progress variables in the reaction zone of a 1-D planar detonation wave. We note that there are only about 8 cells for the fast SURF reaction. At this resolution there is some burning in the shock rise. The adaptive mesh uses coarser zones for the carbon clustering reaction. Due to the slower rate, it is fairly well resolved.

An important point for the calibration simulations is that the shock pressure critical for both the Pop plot and failure diameter simulations is in the range of 15 to 18 GPa, which is less than half the von Neumann spike pressure for a planar detonation. Consequently, the SURF rate is over an order of magnitude lower (see fig. 2). Thus, the resolution requirement for the calibration simulations is much less than is needed to resolve the fast part of the reaction zone for a propagating CJ detonation wave.

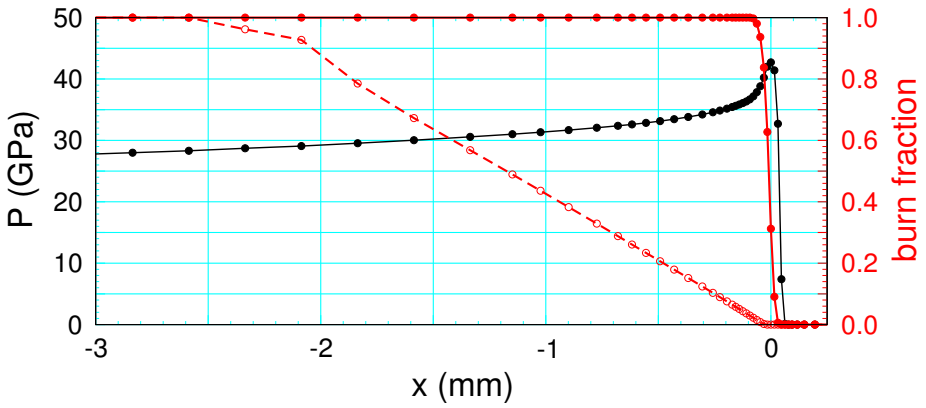

Figure 4: Planar detonation wave profile for ambient PBX9502. Solid and dashed red curves correspond to burn fraction for the fast hot spot (SURF) rate and the slow carbon clustering (SURFplus) rate, respectively. Circle denote grid cells. Profiles have been shifted such that lead shock is at $x = 0$.

3.1 Calibration data

The Pop plot data used in the calibration are shown in fig. 5. Previous calibration for ambient PBX 9502 [Menikoff, 2017c] used the dashed black curve. This has the unexpected property that it crosses the hot Pop plot curve just under 25 GPa. For the present calibration we use the solid black curve. We note that both curves are within the scatter in the data, and that the crossing occurs when the fits to the data are extrapolated.

All three Pop plot curves (hot, ambient and cold) are based on the same measurement technique using gas gun experiments. The previous ambient Pop plot data used wedge experiments. The model calibration fits the Pop plot in the range $8 < P_s < 15$ to within 2 per cent. This is much less than the scatter in the data points upon which the linear fits are based; see for example [Gustavsen et al., 2006, Fig. 10]. We note that each data point corresponds to an experiment with a new PBX sample, and that part of the scatter in the data is due to variations among samples of heterogeneities at the grain scale, which affects the hot-spot burn rate.

The failure diameter simulations are similar to those described in [Menikoff, 2017c]. For the calibrated parameters, table 3 lists the results for the failure diameter and the limiting detonation speed. The failure diameter decreases significantly with increasing temperature; about a factor of 2 between hot and cold PBX 9502. We note that the failure diameter also varies with lot. In contrast to the failure diameter there is little change in the limiting detonation speed. This is due to 2 offsetting effects. First, the larger rate at higher temperatures reduces the curvature effect. Second, the larger rate decreases the failure diameter which increases the front curvature.

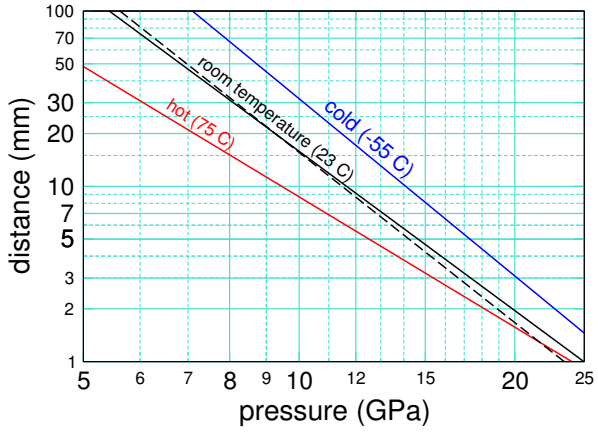

$\log_{10}(x/mm) = a - b\log_{10}(P/GPa)$

T(C)	a	b	reference
76	3.41	2.47	Gustavsen et al. [2017]
23	4.22	3.02	Gustavsen et al. [2006]
-55	4.59	3.19	Gustavsen et al. [2012]

Figure 5: Pop plots for hot, ambient and cold PBX 9502. Curves shown are extrapolated slightly outside range of data; about $8 < P < 15$ GPa. Dashed curve [Gibbs and Popolato, 1980, §7.2] used in previous calibration of ambient PBX 9502.

Table 3: Simulated failure diameter and limiting detonation speed for PBX 9502. Experimental detonation speed for lot 79-04 is from [Campbell, 1984].

radius (mm)	D (km/s)	D_{exp} (km/s)
hot		
2.5	fails	
3.0	7.35	7.38
ambient		
4.0	fails	
4.5	7.44	7.46
cold		
5.0	fails	
5.5	7.42	7.42

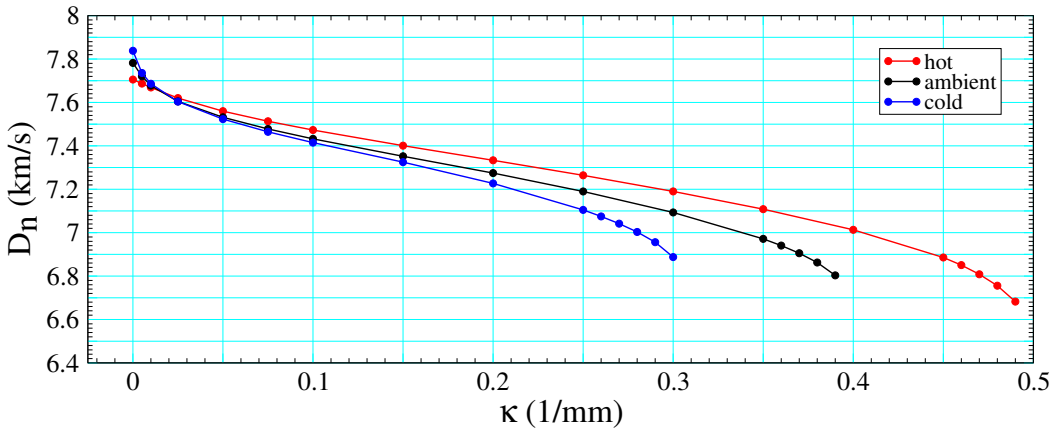

Figure 6: $D_n(\kappa)$ for hot, ambient and cold PBX 9502 from the quasi-steady detonation profile ODEs.

The curvature effect can be determined from ODEs for the 1-D quasi-steady detonation profile; in the context of the SURFplus model see [Menikoff and Shaw, 2012]. Figure 6 shows the model $D_n(\kappa)$ curves for hot, ambient and cold PBX 9502. The curves have a steep slope for $\kappa < 0.05\,\text{mm}^{-1}$ and then a lower slope for larger κ. Another important property is the variation with initial temperature. For small κ, the curves are ordered by the CJ detonation speed; *i.e.*, for fixed κ, D_n decreases with increasing temperature due to the decrease in initial density. While for large κ, the curves are in the opposite order. They cross around $\kappa = 0.025\,\text{mm}^{-1}$.

These properties are due to the fast-slow reaction rate of TATB, which results in a variation of the reaction-zone width to the sonic point and the amount carbon clustering energy released

up to the sonic that contributes to driving the curved detonation wave. For $\kappa < 0.05\,\mathrm{mm}^{-1}$, the fast hot-spot reaction has run to completion ($\lambda_1 = 1$), and the sonic point is in the region with a significant amount of the slow carbon clustering reaction; see fig. 4. For larger curvature, the sonic point is near the end of the fast reaction. To match the order of the curves with initial temperature for $\kappa > 0.05\,\mathrm{mm}^{-1}$, we needed to increase the slow rate by decreasing the parameter t_2 with increasing temperature.

For the ambient temperature, a comparison of the curvature effect from the model, simulation and experiment is shown in fig. 7. The $D_n(\kappa)$ curve for the model is based on the quasi-steady detonation profile ODEs, and the curves for the simulation and experiments are based on the shape of the detonation front for an unconfined rate stick using the analysis described in [Hill et al., 1998]. There are 3 cases for the experimental data. The closest comparison with the failure diameter simulation is for the 10 mm diameter rate stick experiment reported in [Hill et al., 1998]. Also shown are fits to data with larger diameter rate sticks for 2 lots [Hill and Aslam, 2010]. One lot corresponds to that used for the diameter effect experiments of Campbell [1984], which is data used to calibrate the model parameters for the failure diameter. The other lot corresponds to the $D_n(\kappa)$ data for the 10 mm diameter rate stick experiment.

The curves are in good agreement for $\kappa \lesssim 0.25\,\mathrm{mm}^{-1}$, but differ significantly for larger κ. As shown in the figure and previously noted, the ODEs for the detonation profile have a solution over a range of κ more limited than the data for either the simulation or the experiments. Experimentally, the larger κ corresponds to the region of the detonation front in the neighborhood

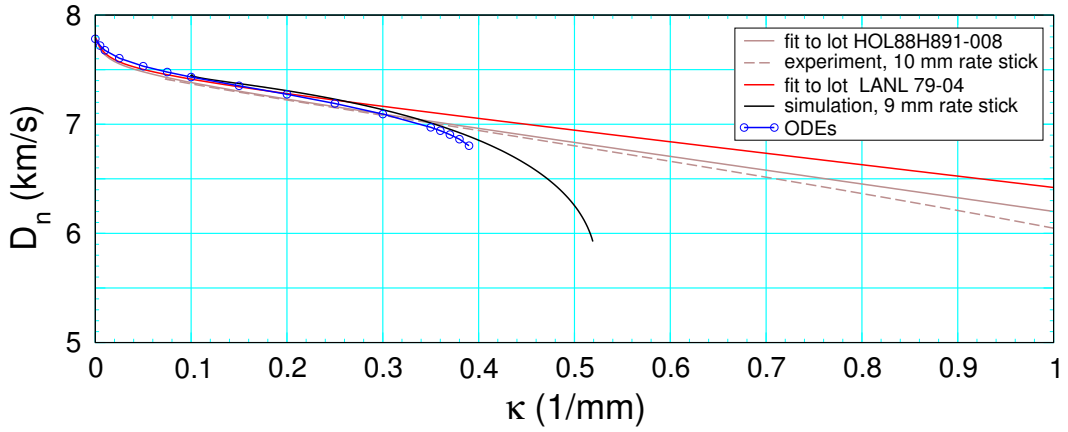

Figure 7: $D_n(\kappa)$ for ambient PBX 9502 from experiments, simulation and the quasi-steady detonation profile ODEs. 10 mm diameter rate stick experiment is for lot HOL88H891-008 [Hill et al., 1998]. Diameter effect experiments used to calibrate rate model are for lot LANL 79-04. $D_n(\kappa)$ fits for both lots are from [Hill and Aslam, 2010].

of the rate stick boundary. As discussed in [Menikoff, 2017c], two issues arise due to the sonic boundary condition at the detonation front.

First, when the sonic point in the reaction zone is near the lead shock, the shock pressure is low compared to the planar von Neumann spike pressure. This greatly reduces the reaction rate, and results in the energy release occurring too far behind the front to drive the lead shock; *i.e.*, the reactive flow along a streamline near the boundary does not correspond to a detonation wave, and the 1-D detonation profile ODEs do not have a solution.

Second in the neighborhood of the boundary there is a large variation in the shock pressure along the front, see fig. 8 The transverse pressure gradient in the reaction zone causes the streamlines to curve and couples neighboring stream tubes; *i.e.*, the approximation of a quasi-steady 1-D reaction zone profile breaks down, and $D_n(\kappa)$ depends on the diameter of the rate stick.

A related issue is that the analysis determining $D_n(\kappa)$ from the shape of the detonation front requires the second derivative of the front position, $\mathsf{d}^2y/\mathsf{d}r^2$. A smooth second derivative is obtained by fitting the front $y(r)$ and taking analytic derivatives of the fitting form. As seen in fig. 9, changes to the fitting parameters that have a barely noticeable effect on the front shape (and are on the order of the uncertainty from the cell size) can have a significant effect on $D_n(\kappa)$. The difference is largest for large κ and occurs in the outter $1/2\,\mathrm{mm}$ of the rate stick; *i.e.*, the neighborhood of the boundary.

These considerations lead us to conclude that a rate model calibration should not be constrained to fit $D_n(\kappa)$ data for large κ. For PBX 9502, the boundary layer effects start around $\kappa = 0.25$ to $0.3\,\mathrm{mm}^{-1}$. We think that the fit shown in fig. 7 covers an adequate range of κ.

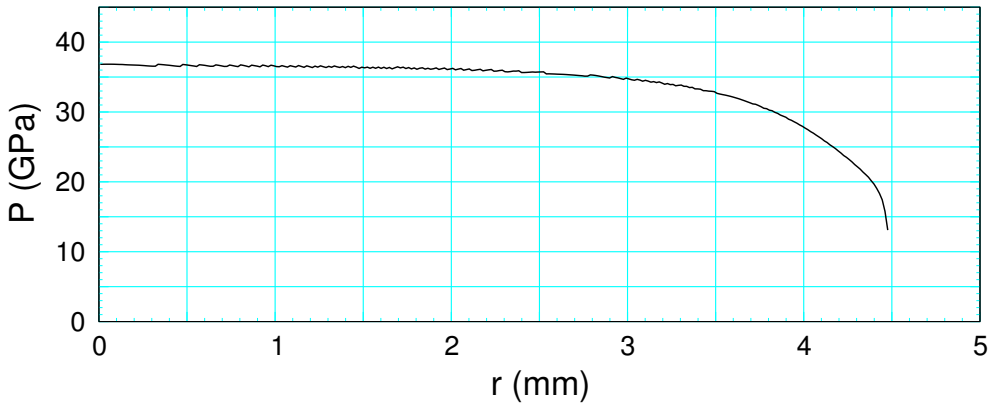

Figure 8: Shock pressure along detonation front from rate stick simulation of ambient PBX 9502.

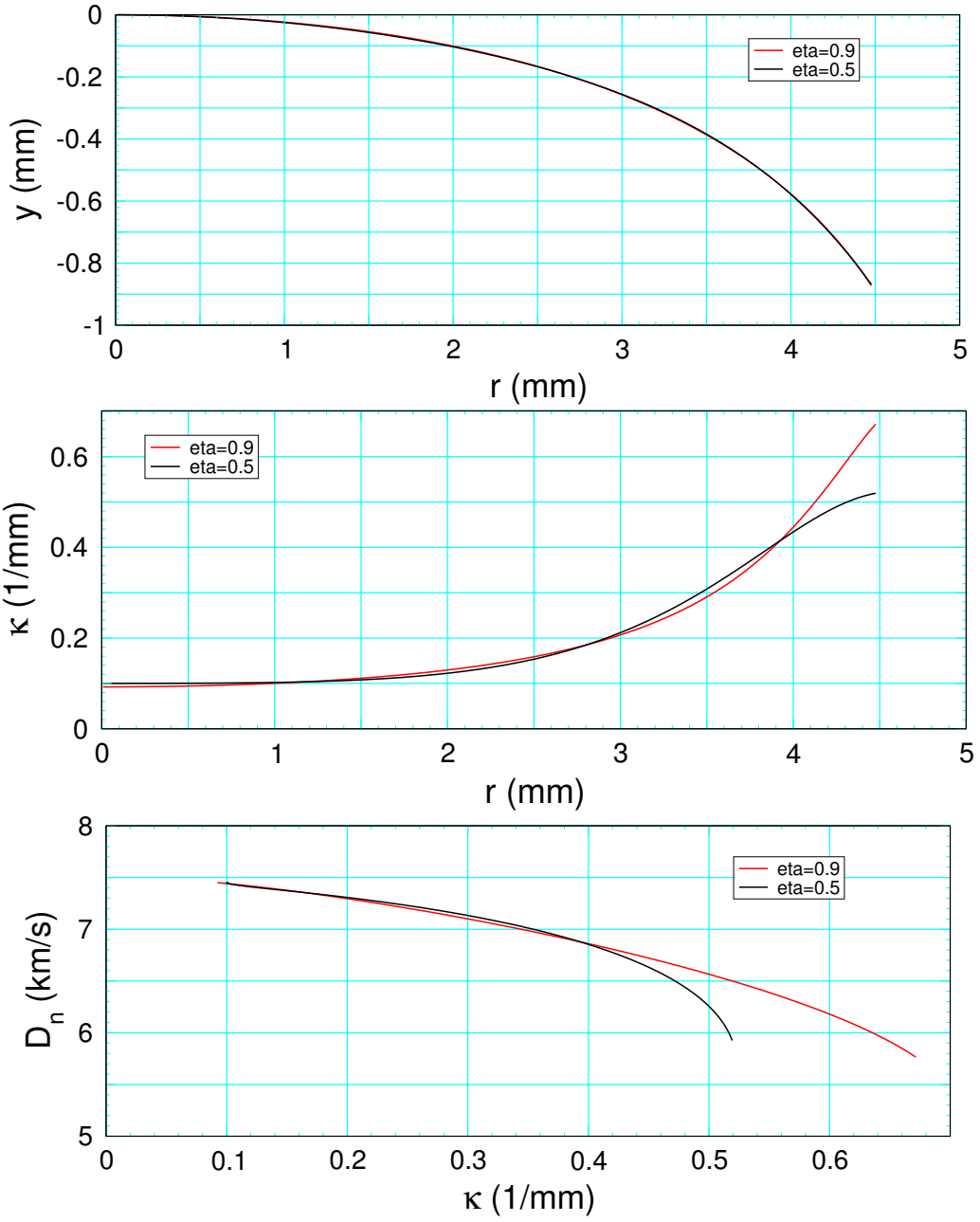

Figure 9: Sensitivity of $D_n(\kappa)$ to fitting the detonation front. Fits to the simulated front shape are shown for two values of the parameter η. See Hill et al. [1998] for the fitting form with parameter η.

3.2 Carbon clustering

The slow SURFplus reaction is motivated by carbon clustering. Recent experiments have measured the cluster radius as a function of time [Watkins et al., 2017, see fig 5] with small angle x-ray scattering. The experiments used a 10 mm diameter cylinder of PBX 9502; *i.e.*, slightly above the failure diameter. Since the x-ray scattering occurs across the cylinder diameter, a complication arises in interpreting the data due to the detonation front curvature. The analysis of the experiments applied a correction by averaging the cluster radius over a diameter based on a simulation of the detonation wave in the cylinder to determine as a function of radius the time difference and radial offset of a fluid particle along a streamline from the detonation front to the axial position of the x-ray beam. The cluster radius along a streamline is based on the diffusion limited clustering model of Shaw and Johnson [1987] using the thermodynamic state from the simulation and the Enskog theory to estimate the viscosity of the detonation products and then applying Stokes-Einstein relation to obtain the diffusion coefficient.

The result of the analysis is that the clustering model is consistent with the data, [Watkins et al., 2017, see fig 7B], assuming an offset time of 75 ns for the start of clustering and a freeze out temperature to cutoff the cluster growth. The freeze out temperature is associated with the thermal energy needed for two clusters to restructure into a single cluster after a collision rather than forming an agglomeration of small clusters. The restructuring is necessary to increase the number of carbon bonds and release chemical energy. The freeze out temperature of about 2500 K depends to some extent on reactive burn model used for the simulation.

From this perspective, it is instructive to look at the flow for the ambient calibration simulation (4.5 mm radius cylinder) just above the failure diameter. Profiles of the reaction progress variables and temperature along streak lines (Lagrangian tracer particles) are shown in fig. 10. For steady state flow, the streak lines correspond to streamlines. On the short spatial and temporal scales of interest, it is sufficient that the reaction zone is quasi-steady.

The first point to note is that the time difference for the fast reaction to mostly complete (say $\lambda_1 = 0.8$) between the axis ($r = 0$) and $r = 3$ mm is about 35 ns, and $r = 4$ mm (0.5 mm from the cylinder boundary) is about 120 ns. For the SURFplus model the carbon clustering reaction time is about 400 ns. However, most of the carbon cluster energy (say 90 %) is released within 200 ns. Consequently, the front curvature has a significant effect when looking across a diameter.

As noted previously [Menikoff, 2017c], the boundary condition for an unconfined cylinder is the sonic pressure on the shock polar. Within 0.5 mm of the cylinder boundary, the lead shock pressure is sufficiently low that the flow along streamlines does not correspond to a quasi-steady detonation profile. There is still reaction, but as seen in the figure, the fast reaction occurs

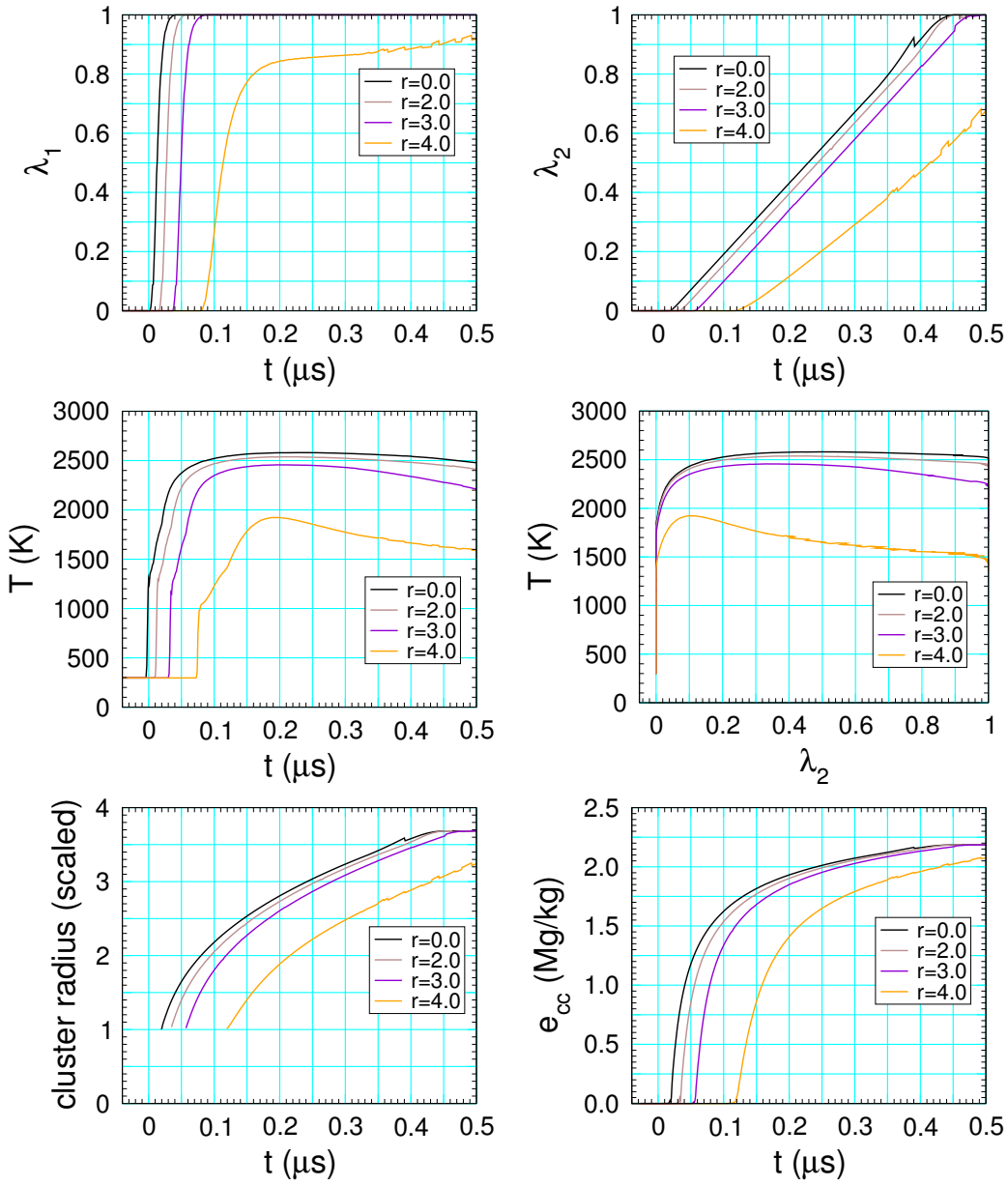

Figure 10: Lagrangian tracer particle profiles of reaction progress variables (λ_1 for hot spot and λ_2 for carbon clustering reactions, respectively) and temperature for 9 mm diameter unconfined rate stick with ambient PBX 9502. Initial tracer particle position are at different radii but fixed axial position near the end of the rate stick when the detonation wave is steady. Time origin has been shifted to the arrival of the detonation front at the tracer particle on the cylinder axis.

significantly slower than for streamlines near the central portion of the cylinder. Also, due to the radial expansion from the boundary, the temperature on the streamlines near the boundary have a peak and then fall off. For these boundary streamlines, the freeze out temperature would significantly limit the cluster size. In addition, the lower temperature may effect the phase of the carbon clusters; diamond or graphite. These effects are not incorporated into the current version of the SURFplus model.

For the central portion of the cylinder, the temperature at the end of the fast reaction is about 2300 K. The SURFplus model assumes that small clusters are formed in the fast reaction, and this contributes several hundred degrees K to the temperature at the end of the fast reaction. For the streamlines with $r < 3$ mm the temperature mostly increases with the carbon clustering reaction; *i.e.*, increasing λ_2. Consequently, a freeze out temperature would not limit the cluster size unless it was a function of cluster size. Physically, the cluster size could also be limited by product radicals binding to the cluster surface. The SURFplus model assumes the cluster radius is given by $(N_{ratio}\,\lambda_2 + 1 - \lambda_2)^{1/3}$, and the cluster energy is proportional to the inverse of the cube root of the radius, Eq. (B.1).

Compared to the analysis of the cluster radius experiments, the SURFplus model starts forming cluster sooner (20 ns relative to the lead front rather than 75 ns), and the bulk of the cluster growth (in term of energy release) is spread out over a longer time (200 rather than 100 to 150 ns). Considering the uncertainty in the analysis due to the measurement of cluster radius averaging across a diameter, the calibrated 9502 SURFplus model is in rough agreement with the carbon cluster data.

4 Summary

The SURFplus reactive burn model has been calibrated for hot (75 C), ambient (25 C) and cold (-77 C) PBX 9502. Thermal expansion with initial temperature is accounted for with a porosity model for the PBX reactants based on an EOS for TATB. For all three cases, the same EOS is used for the products and for the TATB. The detonation states are listed in table 1.

The burn rate parameters are calibrated to Pop plot data, failure diameter and limiting detonation speed, and the curvature effect. The parameters for the three cases are listed in table 2. For convenience of the reader, the equations defining the SURF model and the SURFplus extension are given in Appendices A and B, respectively.

Model calibration involves fitting parameters based on comparing experimental and simulated data. Mesh resolution can affect the accuracy of simulations due to the narrow reaction

zone. For example, the detonation speed in the cylinder test can be 1 to 2 per cent low if the reaction zone is under-resolved [Menikoff, 2014].

For the calibration simulations, we used the `xRage` code. Utilizing its adaptive grid refinement capability, a refined cell size of 0.015 mm is used for the fast SURF reaction. This is expected to be sufficient for the failure diameter. We plan on examining the issue of the resolution needed for the failure diameter simulations in a future report.

For the curvature effect, $D_n(\kappa)$ is computed from both the ODEs for the 1-D quasi-steady detonation profile and from the shape of the detonation front from 2-D simulations for an unconfined rate stick. The two methods and experimental data agree for small curvature; $\kappa < 0.25\,\mathrm{mm}^{-1}$. As noted previously [Menikoff, 2017c], the larger curvature occurs in the neighborhood of the boundary of the rate stick where the assumptions for a 1-D quasi-steady profile break down. Moreover, for large curvature the experimental data depends on the diameter of the rate stick. Consequently, a reactive burn model can only fits $D_n(\kappa)$ for small curvature.

APPENDICES

A SURF rate

The reaction progress variable for the SURF model (fast hot-spot reaction) is determined as a function of a dimensionless reaction-scale variable s and a reaction-scale function $g(s)$, see [Menikoff, 2017c] and references therein;

$$\lambda = g(s) \ , \tag{A.1a}$$

$$\frac{\mathsf{d}}{\mathsf{d}t} s = \tilde{f}(p_s, p) = f(p_s) \cdot \begin{cases} 0 \ , & \text{for} \quad p \le 0 \\ \left[\frac{p}{p_s}\right]^n \ , & \text{for } 0 < p < p_s \\ \left[\frac{p}{p_s}\right]^{n_{hi}} \ , & \text{for } p_s \le p \end{cases} \ , \tag{A.1b}$$

where $f(p_s)$ is a shock-strength function representing the number density of hot spots activated by the lead shock, n and n_{hi} are model parameters, and p_s is the shock pressure from the shock detector algorithm, see [Menikoff, 2016]. In addition, $f(p_s)$ is taken to be zero unless a shock is detected or $p_s > p_{burn}$, where p_{burn} is a threshold pressure parameter to start burning introduced in [Menikoff, 2016].

The fitting forms used for the reaction-scale function is taken to be

$$g(s) = 1 - exp(-s^2) \ . \tag{A.2}$$

This can be associated with cylindrically expanding deflagration wavelets from randomly distributed hot spots. It gives a good fit to the profile shape of embedded velocity gauge data for shock-to-detonation transition experiments; see [Menikoff, 2015].

With pressure and time scales p_{scale} and t_{scale}, respectively, the fitting form for the shock-strength function is given by

$$f(p_s) = \begin{cases} 0 & \text{for} \quad p_s \le p_0, \\ c_{low}\left[\frac{p_s - p_0}{p_{\text{scale}}}\right]^{fn_{low}} & \text{for } p_0 < p_s \le p_{low}, \\ c\left[\frac{p_s}{p_{\text{scale}}}\right]^{fn} & \text{for } p_{low} < p_s \le p_1, \\ f(p_1) \cdot \exp\left[fn \cdot \ln(p_s/p_1) \cdot (1 - B_2 \ln(p_s/p_1))\right] & \text{for } p_1 < p_s \le p_{hi} \\ f_{max} & \text{for } p_{hi} < p_s \ . \end{cases} \tag{A.3}$$

With derived parameters

$$
\begin{aligned}
fn_{low} &= \left[1 - p_0/p_{low}\right] fn \ , \\
c_{low} &= c \cdot (p_{low}/p_{\text{scale}})^{fn} \cdot \left[\frac{p_{\text{scale}}}{p_{low} - p_0}\right]^{fn_{low}} \ , \\
B_2 &= \frac{1}{2\ln(p_{hi}/p_1)} \ , \\
f_{max} &= f(p_1) \exp\left[\tfrac{1}{2} f_n \ln(p_{hi}/p_1)\right] \ ,
\end{aligned}
$$

f and f' are continuous at the end points of the pressure intervals; p_0, p_{low}, p_1, p_{hi}.

The current form for $f(p_s)$ has 4 pressure transition points (p_0, p_{low}, p_1, p_{hi}) and 3 dimensionless parameters $C = c \cdot t_{\text{scale}}$, f_n and n.

B SURFplus extension

The SURFplus model [Menikoff and Shaw, 2012] adds a second reaction progress variable, λ_2, to account for the energy release from carbon clustering. The carbon cluster energy is given by

$$
e_{CC}(\lambda_2) = \left(\left[\lambda_2 \, N_{\text{ratio}} + (1 - \lambda_2)\right]^{-1/3} - N_{\text{ratio}}^{-1/3} \right) Q \ , \tag{B.1}
$$

where Q and N_{ratio} are model parameters with dimensions of specific energy and dimensionless, respectively. The rate equation for λ_2 is

$$
\mathsf{d}\lambda_2/\mathsf{d}t = \lambda^2 h'\big(h^{-1}(\lambda_2)\big) \ , \tag{B.2}
$$

where $h(t)$ is a model function for the limiting time dependence of λ_2 in a steady CJ detonation wave, $h' = \mathsf{d}h/\mathsf{d}t$ and h^{-1} is the inverse function of h; *i.e.*, if $h(t) = \lambda_2$ then $h^{-1}(\lambda_2) = t$.

The pressure for the SURFplus model is determined by subtracting out the carbon cluster energy from the equilibrium EOS; *i.e.*,

$$
\widetilde{P}(V, e, \lambda, \lambda_2) = P(V, e - \lambda \, e_{CC}(\lambda_2), \lambda) \ , \tag{B.3}
$$

where $P(V, e, \lambda)$ is the mixture EOS for the SURF model.

The limiting carbon cluster reaction function is defined by 4 parameters: t_1 and t_2 with dimensions of time, and dimensionless parameters h_1 and h_2. The fitting form is

$$h(t) = \begin{cases} \frac{1}{2}\, a_1\, t^2 \ , & \text{for } 0 < t \le t_1 \\ h_1 + \left[(h_2 - h_1)/(t_2 - t_1)\right](t - t_1) \ , & \text{for } t_1 < t \le t_2 \\ 1 - \frac{1}{2}\, a_3\, (t_3 - t)^2 \ , & \text{for } t_2 < t \le t_3 \\ 1 \ , & \text{for } t_3 < t \end{cases} \tag{B.4}$$

where

$$a_2 = (h_2 - h_1)/(t_2 - t_1) \tag{B.5a}$$

$$t_1 = 2\, h_1/a_2 \tag{B.5b}$$

$$a_1 = 0.5\, a_2^2/h_1 \tag{B.5c}$$

$$t_3 = t_2 + 2\,(1 - h_2)/a_2 \tag{B.5d}$$

$$a_3 = 0.5\, a_2^2/(1 - h_2) \tag{B.5e}$$

By construction, $h(t)$ is linear in the range between h_1 and h_2, and h and $\mathsf{d}h/\mathsf{d}t$ are continuous at t_1 and t_2.

We note that $h'(0) = 0$. Therefore, $\lambda_2 = 0$ is a fixed point of Eq. (B.2). To get around this, we express $\lambda_2 = s_2^2$. The transformed rate equation for s_2,

$$\frac{\mathsf{d}}{\mathsf{d}t} s_2 = \tfrac{1}{2}\lambda^2 \begin{cases} \frac{h_1 a_2}{h_1 s_2 + (t_1 a_2 - h_1)(h_1^{1/2} - s_2)} \ , & \text{for } s_2^2 < h_1 \ ; \\ a_2/s_2 \ , & \text{for } h_1 \le s_2^2 \le h_2 \ ; \\ [2(1 - s_2^2)\, a_3]^{1/2}/s_2 \ , & \text{for } h_2 < s_2^2 \ ; \end{cases} \tag{B.6}$$

is then regular at the start of the carbon clustering reaction.

References

A. W. Campbell. Diameter effect and failure diameter of a TATB based explosive. *Propellants, Explosives, Pyrotechnics*, 9:183–187, 1984. URL http://dx.doi.org/10.1002/prep.19840090602. 3, 7, 12, 13

J. J. Dick, C. A. Forest, J. B. Ramsay, and W. L. Seitz. The Hugoniot and shock sensitivity of a plastic-bonded TATB explosive PBX 9502. *J. Appl. Phys*, 63:4881–4888, 1988. URL http://dx.doi.org/10.1063/1.340428. 3

W. Fickett and W. C. Davis. *Detonation*. Univ. of Calif. Press, 1979. 7

T. R. Gibbs and A. Popolato, editors. *LASL Explosive Property Data*. Univ. of Calif. Press, 1980. URL http://lib-www.lanl.gov/ladcdmp/epro.pdf. 2, 11

L. Green, E. Lee, A. Mitchell, and C. Tarver. The supra-compression of LX-07, LX-17, PBX-9404, and RX-26-AF and the equation of state of the detontion products. In *Eighth Symposium (International) on Detonation*, pages 587–595, 1985. 3

R. L. Gustavsen, S. A. Sheffield, and R. R. Alcon. Measurements of shock initiation in the tri-amino-tri-nitro-benzene based explosive PBX 9502: Wave forms from embedded gauges and comparison of four different material lots. *J. Appl. Phys.*, 99:114907, 2006. URL http://dx.doi.org/10.1063/1.2195191. 2, 3, 11

R. L. Gustavsen, R. J. Gehr, S. M. Bucholtz, R. R. Alcon, and B. D. Bartram. Shock initiation of triaminotrinitrobenzene base explosive PBX 9502 cooled to -55 C. *J. Appl. Phys.*, 112, 2012. URL http://dx.doi.org/10.1063/1.4757599. 11

R. L. Gustavsen, R. J. Gehr, S. M. Bucholtz, A. H. Pacheco, and B. D. Bartram. Shock initiation of the TATB-based explosive PBX 9502 heated to 76 C. In *AIP Conference Proceedings 1793, 030017*, 2017. URL http://dx.doi.org/10.1063/1.4971475. 11

L. G. Hill and T. D. Aslam. Detonation shock dynamics calibration for PBX 9502 with temperature, density and material lot variation. In *Proceeding of the Fourteenth International Symposium on Detonation*, pages 779–788, 2010. 2, 13

L. G. Hill, J. B. Bdzil, and T. D. Aslam. Front curvature rate stick measurements and detonation shock dynamics calibration for PBX 9502 over a wide temperature range. In *Proceeding of the Eleventh International Symposium on Detonation*, pages 1029–1037, 1998. 13, 15

J. R. Kolb and H. F. Rizzo. Growth of 1,3,5-triamino-2,4,6-trinitrobenzene (TATB) I. Anisotropic thermal expansion. *Propellants and Explosives*, 4:10–16, 1979. URL http://dx.doi.org/10.1002/prep.19790040104. 4

R. Menikoff. Complete EOS for PBX 9502. Technical Report LA-UR-09-06529, Los Alamos National Lab., 2009. URL http://www.osti.gov/scitech/servlets/purl/1043481/. 2, 3, 4

R. Menikoff. Effect of resolution on propagating detonation wave. Technical Report LA-UR-14-25140, Los Alamos National Laboratory, 2014. URL http://dx.doi.org/10.2172/1136940. 19

R. Menikoff. Shock-to-detonation transition simulations. Technical Report LA-UR-15-25266, Los Alamos National Lab., 2015. URL http://www.osti.gov/scitech/servlets/purl/1193613/. 20

R. Menikoff. Shock detector for SURF model. Technical Report LA-UR-16-20116, Los Alamos National Lab., 2016. URL http://www.osti.gov/scitech/servlets/purl/1234496. 20

R. Menikoff. SURFplus model calibration strategy. Technical Report LA-UR-17-22073, Los Alamos National Lab., 2017a. URL https://www.osti.gov/scitech/servlets/purl/1346849. 8

R. Menikoff. Fine tuning the CJ detonation speed of a high explosive products equation of state. Technical Report LA-UR-17-23912, Los Alamos National Lab., 2017b. URL https://www.osti.gov/scitech/servlets/purl/1357103. 3

R. Menikoff. Failure diameter of PBX 9502: Simulations with the SURFplus model. Technical Report LA-UR-17-25300, Los Alamos National Lab., 2017c. URL https://www.osti.gov/scitech/servlets/purl/1369155. 2, 3, 10, 11, 14, 16, 19, 20

R. Menikoff and M. S. Shaw. The SURF model and the curvature effect for PBX 9502. *Combustion Theory And Modelling*, pages 1140–1169, 2012. URL http://dx.doi.org/10.1080/13647830.2012.713994. 2, 12, 21

H. F. Rizzo, J. R. Humphrey, and J. R. Kolb. Growth of 1,3,5-triamino-2,4,6-trinitrobenzene (TATB) II. Control of growth by use of high t_g polymeric binders. *Propellants and Explosives*, 6:27–36, 1981. URL http://dx.doi.org/10.1002/prep.19810060202. 4

M. S. Shaw and J. D. Johnson. Carbon clustering in detonations. *J. Appl. Phys.*, 62:2080–2085, 1987. 9, 16

C. B. Skidmore, T. A. Butler, and C. W. Sandoval. The elusive coefficient of thermal expansion in PBX 9502. Technical report, Los Alamos National Lab., January 2003. LA-14003, https://www.osti.gov/scitech/servlets/purl/809945. 2, 3, 4, 5

P. C. Souers, P. Lewis, M. Hoffman, and B. Cunningham. Thermal expansion of LX-17, PBX 9502 and ultrafine TATB. *Propellants, Explosives, Pyrotechnics*, 36:335–340, 2011. URL http://dx.doi.org/10.1002/prep.201000119. 4

P. K. Tang, W. W. Anderson, J. N. Fritz, R. S. Hixson, and J. E. Vorthman. A study of the overdriven behaviors of PBX 9501 and PBX 9502. In *Eleventh Symposium (International) on Detonation*, pages 1058–1064, 1998. 3

E. B. Watkins, K. A. Velizhanin, D. M. Dattelbaum, T. D. Aslam, D. W. Podlesak, R. C. Huber, M. A. Firestone, B. S. Ringstrand, T. M. Willey, M. Bagge-Hansen, R. Hodgin, L. Lauder, T. van Buuren, N. Sinclair, P. A. Rigg, S. Seifert, and T. Gog. Evolution of solid carbon nanoparticles in the detonation products of PBX 9502. *J. Phys. Chem. C*, submitted, 2017. 16